applied sciences

MDPI

Article

Operando XAS of a Bifunctional Gas Diffusion Electrode for Zn-Air Batteries under Realistic Application Conditions

Emanuele Marini [1], Danilo Oliveira De Souza [2], Giuliana Aquilanti [2], Michael Liebert [1], Francesca Rossi [3] and Benedetto Bozzini [4,*]

[1] Zentrum für Sonnenenergie- und Wasserstoff-Forschung Baden-Württemberg (ZSW), Helmholtzstraße 8, 89081 Ulm, Germany; emanuele.marini@zsw-bw.de (E.M.); michael.liebert@zsw-bw.de (M.L.)
[2] Elettra-Sincrotrone Trieste S.C.p.A., S.S. 14-km 163.5 in Area Science Park, 34149 Basovizza, Italy; danilo.oliveiradesouza@elettra.eu (D.O.D.S.); giuliana.aquilanti@elettra.eu (G.A.)
[3] Department of Innovation Engineering, University of Salento, Via Monteroni, 73100 Lecce, Italy; francesca.rossi@studenti.unisalento.it
[4] Department of Energy, Politecnico di Milano, Via Lambruschini 4, 20156 Milano, Italy
* Correspondence: benedetto.bozzini@polimi.it

Abstract: In this study, operando X-ray absorption spectroscopy (XAS) measurements were carried out on a newly developed O_2 bi-functional gas diffusion electrode (GDE) for rechargeable Zn-air batteries, consisting of a mixture of α-MnO_2 and carbon black. The architecture and composition of the GDE, as well as the electrochemical cell, were designed to achieve optimum edge-jumps and signal-to-noise ratio in the absorption spectra for the Mn K-edge at current densities that are relevant for practical conditions. Herein, we reported the chemical changes that occur on the MnO_2 component when the GDE is tested under normal operating conditions, during both battery discharge (ORR) and charge (OER), on the background of more critical conditions that simulate oxygen starvation in a flooded electrode.

Keywords: Zn-Air; Operando XAS; Bifunctional Gas Diffusion Electrode; ORR; OER

check for updates

Citation: Marini, E.; Oliveira De Souza, D.; Aquilanti, G.; Liebert, M.; Rossi, F.; Bozzini, B. Operando XAS of a Bifunctional Gas Diffusion Electrode for Zn-Air Batteries under Realistic Application Conditions. *Appl. Sci.* **2021**, *11*, 11672. https://doi.org/10.3390/app112411672

Academic Editor: Aliaksandr Shaula

Received: 18 October 2021
Accepted: 2 December 2021
Published: 9 December 2021

Publisher's Note: MDPI stays neutral with regard to jurisdictional claims in published maps and institutional affiliations.

Copyright: © 2021 by the authors. Licensee MDPI, Basel, Switzerland. This article is an open access article distributed under the terms and conditions of the Creative Commons Attribution (CC BY) license (https://creativecommons.org/licenses/by/4.0/).

1. Introduction

In order to apply strategies for the rational design of bi-functional oxygen reduction reaction (ORR—discharge mode) and oxygen evolution reaction (OER—charge mode) catalysts for metal-air batteries, it is important to improve our understanding of the chemical and structural characteristics of the active material under reaction conditions. In this field, in recent years, X-ray absorption spectroscopy (XAS) is becoming increasingly popular because it can be combined with electrochemistry to elucidate the properties of catalytic materials in situ and operando. XAS can be separated into X-ray absorption near edge structure (XANES) and the extended X-ray absorption fine structure (EXAFS). The former provides information on the electronic structure of the catalyst, while the latter assesses the interatomic distances and coordination numbers of the atoms (i.e., the chemical environments) that constitute the catalysts. XAS studies have been formerly applied in situ to a number of ORR and OER catalyst systems. Manganese-based oxides (Mn-oxides) are among the most active electrocatalysts for the ORR and the most studied using XAS-based methods for alkaline metal-air batteries. Mn oxides exist in a large variety of structures, where the Mn ions can have a wide range of valence states, typically from 2+ to 4+ [1], exhibiting different catalytic activities for the ORR and OER kinetics. Ex situ and in situ XAS at the Mn K-edge (hard XAS) and the Mn $L_{3,2}$-edges (soft XAS) have been used in a number of investigations to correlate Mn valence with OER and ORR activity, and Risch et al. [1] have provided a comprehensive overview of these studies. It is worth noting that, in most of the cases reported in the literature, owing to cell and time constraints, in situ and operando XAS measurements (for a distinction of the two approaches, see [2]) were carried

out under experimental conditions that are far from realistic. Typical measured current densities are two to three orders of magnitude smaller than those used in actual metal-air battery applications [1,3,4] (e.g., $j_{ORR} = -0.01$ mA·cm^{-2} vs. -10 mA·cm^{-2}). Furthermore, the majority of operando XAS studies worked under potentiostatic conditions, while real batteries generally function in a galvanostatic mode.

In the present investigation, we conducted in situ XAS measurements of a newly developed O_2 bi-functional gas diffusion electrode (GDE) made of α-MnO_2 nanowires (NWs), obtained from a facile synthesis method, combined with commercially available carbon black. Both the architecture and composition of the electrode, as well as the configuration of the electrochemical setup, have been designed to achieve optimal edge-jumps and signal-to-noise ratio in the absorption spectra for the XAS Mn K-edge, without sacrificing the current densities applied during testing (electrode performance). In this way, we could perform high-quality operando XAS spectroscopy under practical GDE operating conditions. We compared the chemical changes that occur on the MnO_2 component when the GDE is tested under normal operating conditions, on the background of more critical conditions that simulate oxygen starvation in a flooded electrode, where the consumption of oxygen is faster than the rate at which oxygen is transported from the gas phase to the catalyst surface.

2. Experimental

2.1. Synthesis of α-MnO_2

α-MnO_2 was synthesized using a microwave-assisted hydrothermal method with a protocol derived from the literature [5]. First, 0.314 g K_2SO_4 (Merck, Emsure®, ACS, ISO, Reag. Ph. Eur), 0.486 g $K_2S_2O_8$ (Fluka, puriss. P.A.), and 0.203 g $MnSO_4 \cdot H_2O$ (Merck, ACS, Reag. Pg Eur) were added with 10 mL distilled water (Milli-Q® water, TKA, water conductivity 18 MΩ·cm) in a 30 mL quartz reaction vial; stirred for 10 min; and then sealed with a PTFE lid. The mixture was then transferred to a microwave reactor (Monowave 400, Anton Paar GmbH) and hydrothermally treated for 10 min at 200 °C. The synthesis product was centrifuged after being washed with deionized water. This process was carried out three times. Finally, the material was vacuum-dried overnight at 60 °C.

2.2. Fabrication of the GDE

In a recent article [6], the fabrication of the gas diffusion electrode (GDE) was reported. A spray-coating method was used to apply the active materials on Toray™ carbon paper that had been pretreated with PTFE. To modify the hydrophobicity/hydrophilicity of the active layer (AL) and gas diffusion layer (GDL), a commercial PTFE suspension (59 wt%, 3M™ Dyneon™ PTFE TF 5060GZ) was employed. To hydrophobize the GDL, the Toray™ carbon paper was soaked for 2 min and 30 s in a solution of distilled water and PTFE suspension, and then dried at room temperature overnight and heat-treated at 330 °C for 30 min. The AL was made using a conventional spray-coating method. An aqueous-alcoholic catalyst solution containing 0.8 wt% commercial PTFE suspension, 53.7 wt% deionized water, 42.5 wt% ethanol (ACS reagent, ≥99.9%, Merck, Darmstadt, Germany), 1.5 wt% commercially available carbon black (C-NERGY SUPER C65, Imerys Graphite & Carbon), and 1.5 wt% α-MnO_2 was used in the corresponding ink. The catalyst-ink solution was stirred for 10 min. The ink was then emulsified for 1 min at 30,000 rpm to ensure optimum particle homogeneity and then sonicated for other 10 min immediately before spray-coating. Finally, several layers of AL were spray-coated on the GDL until an active material loading of 7.6 mg·cm^{-2} was achieved. The AL composition was 3.0 mg·cm^{-2} α-MnO_2, 3.0 mg·cm^{-2} carbon black, and 1.6 mg·cm^{-2} PTFE. The composition of the air electrode was adapted to ensure optimal absorption (edge-jump) at the corresponding XAS Mn K-edge energy (6.539 keV) of ~0.5 (see Figure 1a).

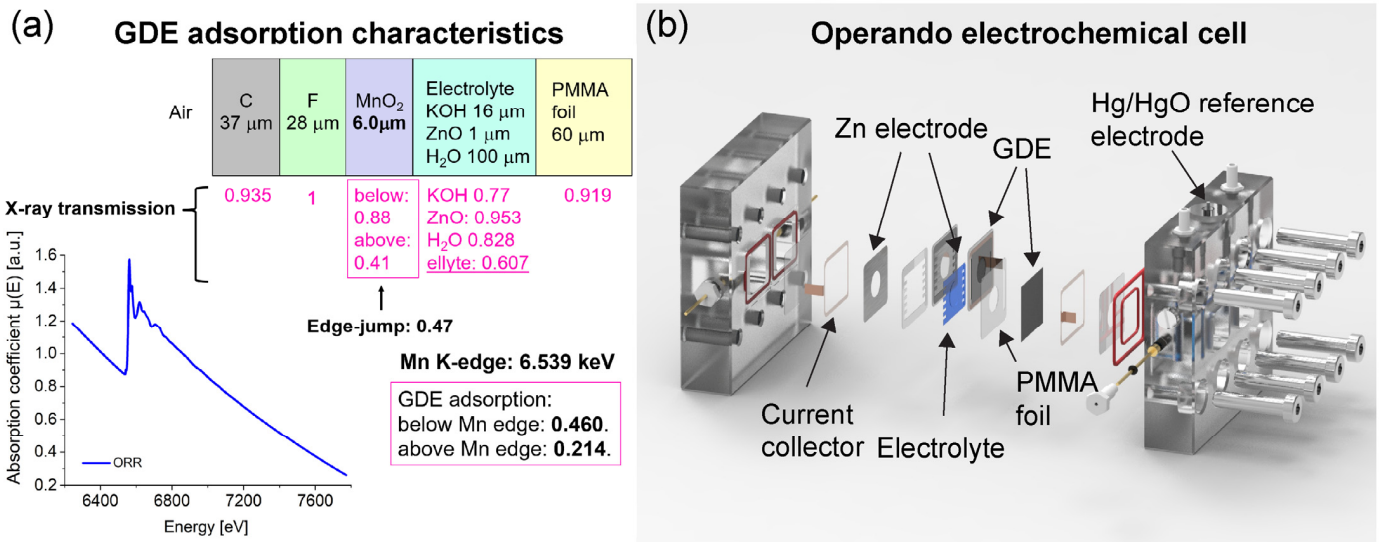

Figure 1. (**a**) X-ray adsorption characteristics at the Mn K-edge energy of the fabricated GDE, together with a raw spectrum acquired operando during ORR. (**b**) Sketch of the operando XAS setup, with the GDE side facing the incoming X-ray beam. Upon transmission through the entire sample, consisting of the GDE, the 6 M KOH electrolyte, and the Zn electrode, part of the X-rays is absorbed by the different materials.

2.3. GDE Testing during Operando XAS

For operando XAS experiments, XAS data were collected using the electrochemical cell illustrated in Figure 1b. The setup is equipped with two parallel Zn-GDE cells, which can be used independently, hence reducing the time needed to switch from one measurement/experiment to another and better exploiting the available beamtime. The setup also includes a channel for the insertion of a reference electrode, which enables to monitor simultaneously the evolution of cathode and anode potentials of one of the two cells. The cell design optimized the XAS spectral quality for the GDE materials, while minimizing the absorption from the other battery (Zn electrode, current collector, electrolyte) and structural materials. Prior to the introduction of the electrolyte (6.0 M KOH) into the cell, a set of XAS measurements was performed on the electrode in the pristine state, scanning the beam over the whole optical window, in order to gain positive information regarding the homogeneity of X-ray absorption across the measured area. After wetting the electrode with the electrolyte, again, several spectra were acquired in the same positions mentioned above, in order to ensure that no signal distortion occurred. After these preliminary steps, XAS measurements were performed, starting with a pristine GDE, under a series of electrochemical conditions, representative of practical battery operation: oxygen reduction (ORR) and oxygen evolution reaction (OER). All operando XAS measurements were carried out in ambient air and by applying a cathodic (for ORR) and an anodic (for OER) current density of j = 5 mA·cm^{-2}, unless otherwise specified. After each change in current density level or sign, the system was allowed to equilibrate for 10 min (to ensure that the system reached a steady-state potential) before starting the acquisition of XAS spectra.

With a ring electron energy of 2.0 GeV and an average current of 310 mA of the Elettra synchrotron light source, yielding a photon flux of ~10^{10} photon·s^{-1} from the bending magnet feeding the XAFS beamline, X-ray absorption spectra (XAS) were recorded [7]. A double-crystal Si (111) monochromator was used to monochromatize the light. The beam size was 20 mm × 1.5 mm (H × V). The XAS data were recorded in transmission mode during electrochemical experiments. An ion chamber in front of the sample was filled with a proper mixture of gases according to the energy of the incidence X-rays, which was used to measure the intensity I_0 of the incident X-rays. After the sample, a second ionization chamber was employed to gather the transmitted intensity I_1. The absorption edge of a Mn foil, which was also measured at the same time, was used to calibrate the energy.

All of the data were obtained at room temperature and at atmospheric pressure. The software Athena [8] was used to carry out data reduction, alignment, merging, deglitching, normalization, and background removal. ARTEMIS [9] was used to perform the EXAFS analysis. The scattering paths for all spectra were produced using the FEFF6 code [10], which used crystallographic data for cryptomelane $K_{1.33}Mn_8O_{16}$ [11].

3. Results and Discussion

To probe structural and chemical-state changes of the MnO_2 electrocatalyst under current loads characteristic of battery operation, operando XAS investigation at the Mn K-edge was carried out. The architecture and composition of the electrode, as well as the configuration of the electrochemical setup and the imposed operating conditions, were those of a real battery, some aspects of which were designed to achieve optimal edge-jumps and signal-to-noise ratio in the absorption spectra for the Mn K-edge, with no impact on the current densities applied during testing and on electrode performance, as detailed in the Experimental Section. The operando XAS experiments, devised to follow discharge/charge cycles, consisting of a sequence of cathodic (ORR) and anodic (OER) current density intervals of j = 5 mA·cm^{-2}, were carried out in ambient air without a CO_2 trap. It should be emphasized that the current densities used in this study are one to two orders of magnitude higher than those reported for other operando XAS studies performed on other GDE design concepts. We thus consider that our results provide information on structural, chemical, and electronic modifications occurring when electrocatalyst material is subjected to application-relevant operating conditions.

The operando XAS experiments were performed on the GDE at three different stages: before (GDE before O_2 starvation), after partial (GDE—partial O_2 starvation, Figure 2 shows the corresponding voltammogram), and after complete O_2 starvation condition (GDE—complete O_2 starvation). OER experiments after complete O_2 starvation were not performed because the interest of the experimental protocol was to assess the chemical state change of Mn resulting from extensive O_2 starving, rather than checking the anodic performance after the GDE has been exposed to such stress conditions. Instead, we believed that it would have been interesting to assess the residual anodic electrocatalytic activity after exposure to milder and more realistic stress conditions. Figure 3a shows the operando X-ray absorption near edge structure (XANES) spectra of the three GDEs at the Mn K-edge. The reference spectra of Mn_3O_4 and pyrolusite MnO_2 powders are also included in the plot. The electrode examined in pristine condition corresponds to the GDE before O_2 starvation (see solid blue and red lines for ORR and OER condition, respectively). It can be seen that the two XANES spectra nearly overlap, with only a minor negative shift (to lower energies) of the rising portion for the spectrum measured at ORR (see blue solid line). The XAS experiment for GDE—partial O_2 starvation was carried out after imposing a short reduction step on the electrode. This was achieved by sealing the GDE with a thin Kapton foil under imposed cathodic polarization at a rate typical of ORR operation (j = −10 mA·cm^{-2}) for about 25 min. These severe operating conditions result in a gradual decrease in electrode potential over time, as shown in Figure 2.

The duration of the reduction process, however, was insufficient to complete the electrochemical reduction of α-MnO_2. When compared with the GDE before O_2 starvation, the equivalent XANES spectra collected at ORR and OER (see blue and red dotted lines) following such partial electrochemical reduction are now clearly moved to lower energies. In the case of bulk metal oxides, a shift in the edge position usually entails a change in the oxidation state of the element, where a shift to lower energies correlates to a reduction of the Mn oxidation state, respectively [3]. The reduction stage was continued for the GDE —complete O_2 starvation until the associated XANES spectrum remained unaltered (no additional shift to lower energy); see black solid line in Figure 3a. It can be noticed that the XANES spectrum coincides with the one of the references Mn_3O_4, thus indicating that, when the access of oxygen to the electrocatalyst is restricted, the α-MnO_2 can be fully transformed into Mn_3O_4. These findings are in agreement with the work of Lima et al. [12]

and Gorlin et al. [3], who demonstrated the formation of the Mn_3O_4 from β-MnO_2 and electrodeposited manganese oxides, respectively, at high ORR overpotentials.

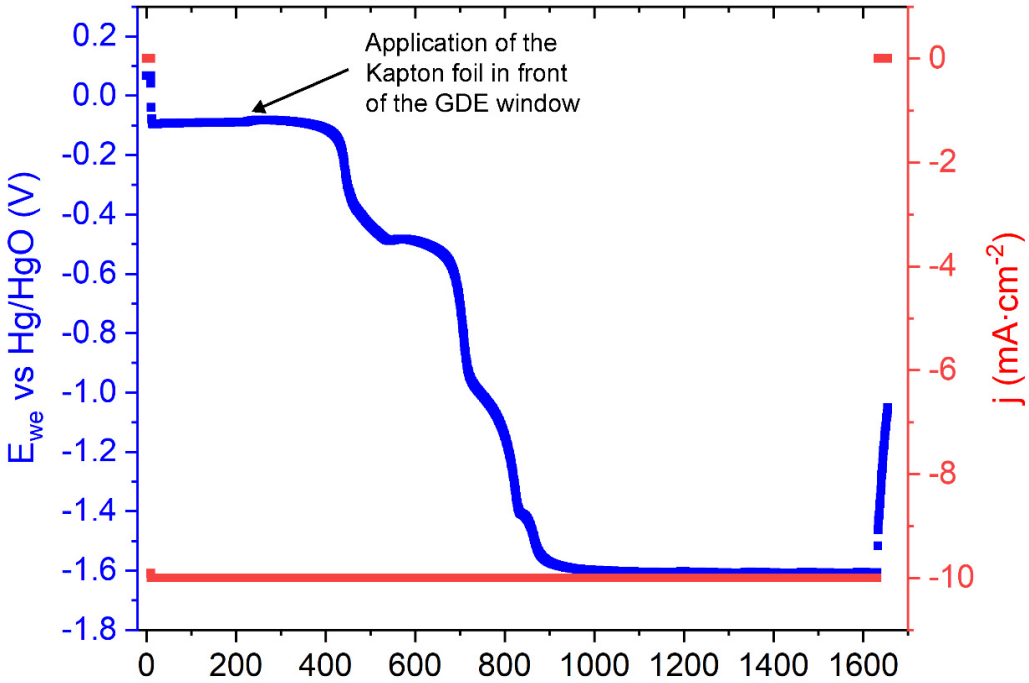

Figure 2. Chronovoltammetry test under ORR condition at j = −10 mA·cm^{-2} before and after application of the Kapton foil in front of the GDE window.

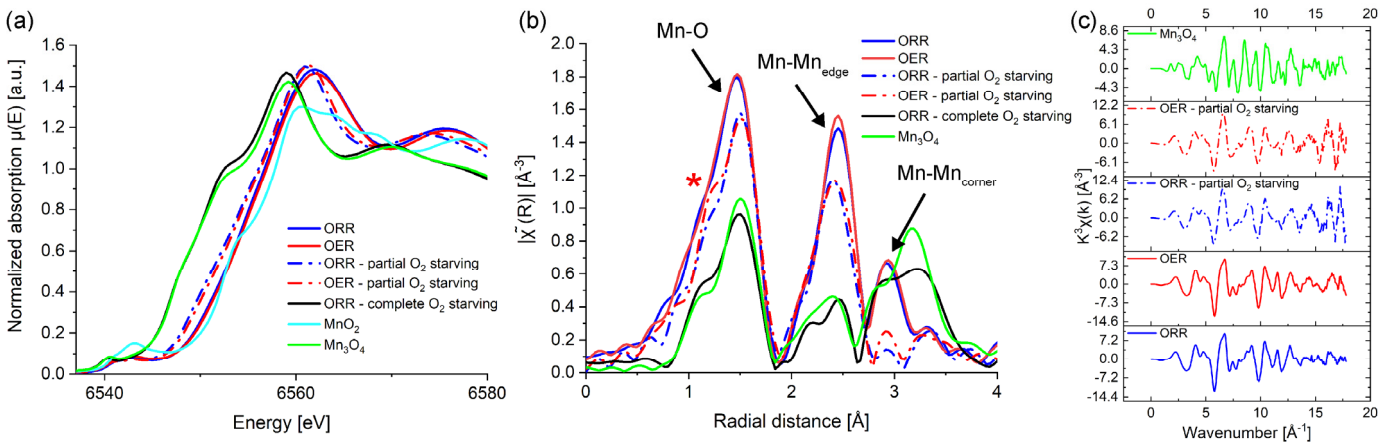

Figure 3. Comparison of (**a**) Mn K-edge XANES and corresponding (**b**) FT amplitudes collected on the GDE before (solid blue and red lines), after partial (dashed blue and red lines), and after complete O_2 starvation (solid black line); the data were not corrected for phase shift. The figure also includes the reference XANES of Mn_3O_4 (lime green) and pyrolusite-type MnO_2 (cyan) powder. (**c**) Same data of Panel (**b**), reported vs. wavenumber in the full measured range.

The local structural evolution of the α-MnO_2 material during the O_2 starvation process is investigated in detail by operando Mn K-edge EXAFS analysis. Figure 3b illustrates the corresponding amplitude of the Fourier transform (FT) of the k^3-weighted Mn K-edge EXAFS oscillations of the GDEs and reference samples shown in Figure 3a. The description of the EXAFS spectrum of α-MnO_2 is partially documented in the literature, but still allows the assignment of characteristic spectral features (see below). Out attribution assignment of EXAFS spectra to cryptomelane, on the one hand, is fully supported by the available literature and, on the other hand, is validated by XRD and Raman measurements of the same samples (dedicated paper in preparation). The typical

FT features of the α-MnO_2 phase are clearly visible for the GDE before O_2 starvation. These include three main peaks: the first peak is related to the Mn-O bonds, the second to the edge-shared Mn-Mn bonds, and the third to the corner-shared Mn-Mn bonds (see Figure 3a). It can be noticed that the FT signal remained relatively unchanged when comparing the ORR and the OER processes, where only the second peak (Mn-Mn_{edge}) shows a small increase under the OER process. Such a weak rise in intensity of the FT peak may be attributed to the formation of additional bonds in the defective manganese oxide lattice [3] or to the depression of local structural disorder [13]. According to Lee et al. [13], FT peak enhancement during the OER process can be regarded as clear evidence of the improved collinear alignment of the MnO_6 octahedra array. The shape and intensity of the FT peaks change drastically after the partial O_2 starvation process. A small shoulder emerges before the main Mn-O FT peak at a radial distance of around 1.1 Å (indicated by a red asterisk in Figure 3b). Furthermore, the FT peak associated with the Mn-Mn_{corner} interaction vanishes, thus indicating a more severe restructuring of the manganese oxide material. The shape and intensity of the FT peaks following complete O_2 starvation match those of Mn_3O_4, confirming the complete transformation of α-MnO_2 into Mn_3O_4.

For the Mn K-edge, variations in the XANES spectrum can be evidently resolved under electrochemical polarization before and after the partial O_2 starvation process. This clearly shows that, when the GDE is reduced in the absence of oxygen, the MnO_2 component undergoes major structural/chemical changes. Quantitative fitting analysis of the EXAFS at the Mn K-edge was used to investigate the evolution of the local chemical environment of the α-MnO_2 during the O_2 starvation process. To perform the fitting analysis on the EXAFS oscillations, we constructed a model starting from the crystal structure of cryptomelane $K_{1.33}Mn_8O_{16}$. The model includes four adsorber–scatterer interactions (also denoted scattering paths), each corresponding to a distinct interatomic distance: two Mn-O interactions and two Mn-Mn interactions. The first scattering path relates to the distance between the Mn ion and the oxygen in the lattice that forms the characteristic MnO_6 octahedra (Mn-$O_{lattice}$). The second Mn-O interaction (Mn-O_{ads}) considers possible adsorbed oxygen-containing species (for instance, intercalated water molecules) [14], as well as hydroxide end groups on the catalyst surface [15]. The last two interactions are associated with the interatomic distances Mn-Mn_{edge} and Mn-Mn_{corner} [13,16]. Systematic variation of the choice and combination of scattering path showed that neglecting one of the Mn-Mn or Mn-O paths leads to a degradation of the fit quality; in particular, subtle, but diagnostic details of the crypomelane structure cannot be followed. To perform the fit of the EXAFS oscillations, the amplitude reduction factor S_0^2 was set to a constant value of 0.8, following the report of Calvin Scott [17]. The edge energy E_0, the mean squared relative displacements σ, the coordination numbers CN, and interatomic distances R were initially set as free variables. Eventually, a second refinement was done to improve the fit quality by constraining those parameters that showed a nearly constant value (to their average value; see quantities in boldface in Table 1). Fitting was carried out in the same R- and k-ranges of 1.25–3.25 Å and 3–15 $Å^{-1}$, respectively. Figure 4a shows the structural model representing the α-MnO_2 that was used to match the EXAFS data (see Experimental Section for more information). Figure 4b shows the comparison of experimental data with the fitted model in R space for the GDE before and after partial O_2 starvation process. Table 1 lists all fitted parameters as a result of the refining method. The fit for both the ORR and OER processes over the analyzed R-range, as shown in Figure 4b, fits well with the experimental results for the GDE before O_2 starvation. Although the quality of the fit for the peak corresponding to the Mn-Mn_{corner} interaction is rather poor after partial O_2 starvation, the peaks corresponding to the Mn-O and Mn-Mn_{edge} interactions still show good agreement between the experimental data and the fit. It is worth noting that the relatively large value of the confidence interval for the Mn-O_{ads} distances—corresponding to intercalation/surface species—with respect to the distances characteristic of the crystal bulk, is due to the

multiplicity of oxygen adsorption sites and adsorbed oxygen-containing species. Instead, the confidence intervals of the other distances considered in our model are in line. An interesting result obtained from the fit is the parameter that corresponds to the coordination number for Mn-$O_{lattice}$ CN(Mn-$O_{lattice}$). This is illustrated in Figure 4c. The value of CN(Mn-$O_{lattice}$) changes considerably according to the condition applied (ORR vs. OER), where it increases during ORR and decreases during OER, respectively. More importantly, when comparing the data before and after O_2 starvation, the value of CN(Mn-$O_{lattice}$) is decreased. This is consistent with a lowering of the average Mn oxidation due to the lack of oxygen supply from ambient air. A parameter that provides more direct information on the relative changes of the average Mn oxidation state is the edge energy E_0. The change in E_0 for the GDE before and after partial O_2 starvation as a function of ORR/OER is shown in Figure 4d. It can be noticed that the value of E_0 decreases by about 5 eV and 3 eV for ORR and OER when comparing before and after O_2 starvation, respectively.

Table 1. Results of non-linear least-squares fittings for the operando EXAFS spectra shown in Figure 4b for electrodes before and after partial O_2 starvation, measured under different electrochemical conditions. Fitting was performed for the following ranges of wavenumbers and radial distances: k = 3.0–15 $Å^{-1}$ and R = 1.25–3.2 Å.

GDE before O_2 Starvation						
Condition	Path	R [Å]	CN	σ^2 [$Å^2$]	E_0 [eV]	R-Factor *
ORR	Mn-O_{ads}	1.620 ± 0.019	**1.0**	0.006 ± 5 × 10^{-4}	6556.6 ± 0.5	0.003
	Mn-$O_{lattice}$	1.896 ± 0.003	7.6 ± 0.3			
	Mn-Mn_{edge}	2.878 ± 0.004	**4.9**	0.006 ± 3 × 10^{-4}		
	Mn-Mn_{corner}	3.439 ± 0.007	**3.7**			
OER	Mn-O_{ads}	1.777 ± 0.027	**1.0**	0.003 ± 6 × 10^{-4}	6557.0 ± 0.5	0.004
	Mn-$O_{lattice}$	1.906 ± 0.004	5.7 ± 0.5			
	Mn-Mn_{edge}	2.879 ± 0.004	**4.9**	0.006 ± 3 × 10^{-4}		
	Mn-Mn_{corner}	3.442 ± 0.008	**3.7**			
GDE after O_2 starvation						
Condition	Path	R [Å]	CN	σ^2 [$Å^2$]	E_0 [eV]	R-Factor *
ORR	Mn-O_{ads}	1.699 ± 0.027	**1.0**	0.003 ± 8 × 10^{-4}	6551.6 ± 0.9	0.008
	Mn-$O_{lattice}$	1.892 ± 0.004	5.8 ± 0.5			
	Mn-Mn_{edge}	2.869 ± 0.006	**6.3**	0.009 ± 4 × 10^{-4}		
	Mn-Mn_{corner}	3.421 ± 0.081	**0.5**			
OER	Mn-O_{ads}	1.768 ± 0.040	**1.0**	0.002 ± 1.1 × 10^{-3}	6553.8 ± 1.3	0.014
	Mn-$O_{lattice}$	1.907 ± 0.009	4.7 ± 0.9			
	Mn-Mn_{edge}	2.875 ± 0.010	**6.3**	0.009 ± 5 × 10^{-4}		
	Mn-Mn_{corner}	3.464 ± 0.097	**0.5**			

Constrained parameters, fixed at the averaged value, are indicated in **bold**. * Paths with similar adsorber–scatterer interactions (i.e., Mn-O_{ads} and Mn-$O_{lattice}$ or Mn-Mn_{edge} and Mn-Mn_{corner}) share the same mean-squared relative displacements: $\sigma^2_{O_{ads}\ \&\ O_{lattice}}$ and $\sigma^2_{Mn-Mn_{edge}\ \&\ Mn-Mn_{corner}}$, respectively. In all curve fitting processes, the goodness of fit was estimated by calculating the averaged R-factor, defined as $\frac{\sum_{i=1}^{3}\left\{\left[\sum_{j=1}^{N}\left(k^i\cdot\chi_{data,\ j}-k^i\cdot\chi_{model,\ j}\right)^2\right]/\left[\sum_{j=1}^{N}\left(k^i\cdot\chi_{data,j}\right)^2\right]\right\}}{3}$.

We used an empirical linear relationship between Mn K-edge energy, E_0, and the Mn oxidation state [3,19] to investigate the oxidation state of the MnO_2 component under starvation conditions (Figure 5). For the calibration, standard Mn compounds MnO (+2), Mn_3O_4 (+2.7 [3]), Mn_2O_3 (+3), and pyrolusite MnO_2 (+4) were utilized. The same figure also shows the Mn valence of α-MnO_2 in its pristine state, which is +3.9. According to the linear relationship, the partial O_2 starvation lowered the valence of Mn to about +3 during ORR and +3.5 during OER. Instead, the Mn oxidation state of GDE before O_2 starvation increased slightly compared with the pristine α-MnO_2 sample, and its value exhibits minor changes between ORR and OER states, thus indicating good reversibility.

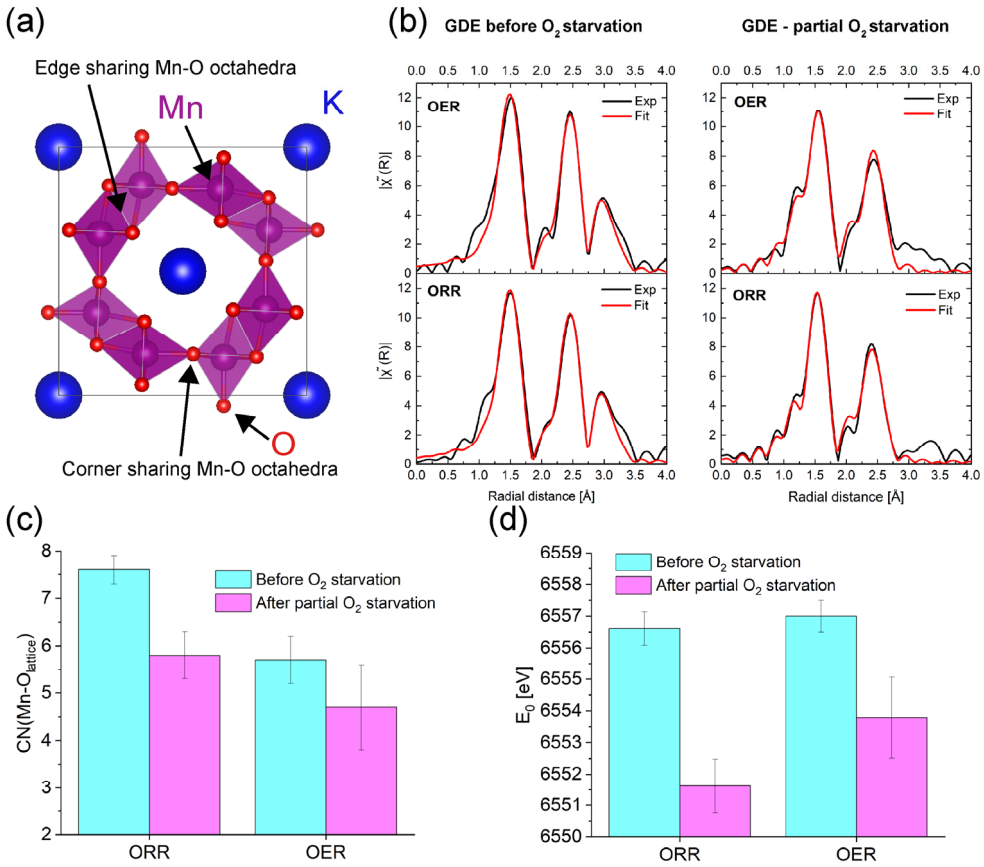

Figure 4. (**a**) Schematic (rendered with the open source software VESTA [18]) showing the crystal lattice of α-MnO_2. (**b**) EXAFS spectra in the R-space (black solid line) and curve fitting (red solid line) of the Mn K-edge for GDE before (left) and after partial O_2 starvation (right) without (left) under OER (top) and ORR (bottom) current loads, as indicated in the figure. (**c**) Mn-$O_{lattice}$ coordination number and (**d**) edge energy E_0 as a function of applied condition.

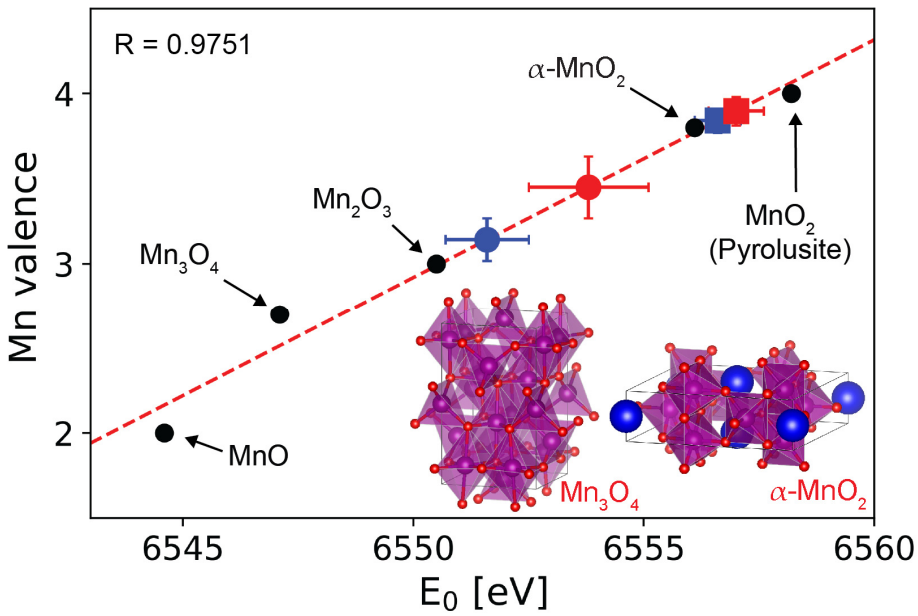

Figure 5. Determination of the α-MnO_2 oxidation state at ORR (blue) and OER (red) conditions before (squared dots) and after (circular dots) partial O_2 starvation of the GDE, using the Mn K-edge energy shift of the reference Mn compounds. See text for details.

4. Conclusions

Operando XAS was employed to probe structural and chemical changes of the α-MnO_2 electrocatalyst embedded into a bifunctional GDE for metal-air batteries. The electrode architecture and composition, as well as the electrochemical setup, were all designed to achieve the optimal edge-jumps and signal-to-noise ratio in the absorption spectra for the Mn K-edge, with no effect on the current densities used, which are suitable for practical GDE operating conditions. The XANES at the Mn K-edge revealed that, when the access of oxygen is restricted to the GDE, the α-MnO_2 is gradually transformed into Mn_3O_4. A quantitative fitting analysis of the EXAFS oscillations was carried out before and after partial O_2 starvation of the GDE, starting from a model based on the crystal structure of cryptomelane α-MnO_2. The fitting results revealed that, after partial O_2 starvation of the GDE, parameters related to edge energy and the number of Mn-O bonds decreased, suggesting a lowering of the average Mn oxidation state. The latter is corroborated by exploiting the phenomenological linear relationship that exists between Mn valence and edge-energy.

This work opens up a new approach to the study of GDEs, based on operando XAS in a complete Zn-air battery, operating under practically relevant conditions, which can enable knowledge-based cell design and definition of charge/discharge protocols.

Author Contributions: Conceptualization, E.M. and B.B.; methodology, E.M., B.B., M.L., F.R.; validation, E.M., B.B., D.O.D.S. and G.A.; formal analysis, E.M. and B.B.; investigation, E.M. and B.B.; data curation, E.M. and B.B.; writing—original draft preparation, E.M. and B.B.; writing—review and editing, E.M., B.B., D.O.D.S. and G.A.; visualization, E.M.; supervision, B.B. All authors have read and agreed to the published version of the manuscript.

Funding: This project was supported by the Federal Ministry of Education and Research, Germany; BMBF, Germany. Grant number: 03SF0499A, LuZi. The synchrotron measurements received User Support from Elettra (beamtime 20185059, PI Benedetto Bozzini).

Institutional Review Board Statement: Not applicable.

Informed Consent Statement: Not applicable.

Conflicts of Interest: The authors declare no conflict of interest.

References

1. Risch, M.; Stoerzinger, K.A.; Han, B.; Regier, T.Z.; Peak, D.; Sayed, S.Y.; Wei, C.; Xu, Z. Shao-Horn Y. Redox Processes of Manganese Oxide in Catalyzing Oxygen Evolution and Reduction: An in Situ Soft X-ray Absorption Spectroscopy Study. *J. Phys. Chem. C* **2017**, *121*, 17682–17692. [CrossRef]
2. Pietsch, P. Wood, X-Ray Tomography for Lithium Ion Battery Research: A Practical Guide. V. *Annu. Rev. Mater. Res.* **2017**, *47*, 451–479. [CrossRef]
3. Gorlin, Y.; Lassalle-Kaiser, B.; Benck, J.D.; Gul, S.; Webb, S.M.; Yachandra, V.K.; Yano, J.; Jaramillo, T.F. In Situ X-ray Absorption Spectroscopy Investigation of a Bifunctional Manganese Oxide Catalyst with High Activity for Electrochemical Water Oxidation and Oxygen Reduction. *J. Am. Chem. Soc.* **2013**, *135*, 8525–8534. [CrossRef] [PubMed]
4. Erickson, E.M.; Thorum, M.S.; Vasic, R.; Marinkovic, S.; Frenkel, A.I.; Gewirth, A.A.; Nuzzo, R.G. In Situ Electrochemical X-ray Absorption Spectroscopy of Oxygen Reduction Electrocatalysis with High Oxygen Flux. *J. Am. Chem.Soc.* **2012**, *134*, 197–200. [CrossRef] [PubMed]
5. Selvakumar, K.; Kumar, S.M.S.; Thangamuthu, R.; Ganesan, K.; Murugan, P.; Rajput, P.; Jha, S.N.; Bhattacharyya, D. Physio-chemical Investigation of Shape-Designed MnO2 Nanostructures and Their Influence on Oxygen Reduction Reaction Activity in Alkaline Solution. *J. Phys. Chem. C* **2015**, *119*, 6604–6618. [CrossRef]
6. Marini, E.; Ludwig, J.; Sylvain, B. Rational design of a low-cost, durable and efficient bifunctional oxygen electrode for rechargeable metal-air batteries. *J. Power Sources* **2021**, *482*, 228900. [CrossRef]
7. Cicco, A.D.; Aquilanti, G.; Minicucci, M.; Principi, E.; Novello, N.; Cognigni, A.; Olivi, L. Novel XAFS capabilities at ELETTRA synchrotron light source. *J. Phys. Conf. Ser.* **2009**, *190*, 012043. [CrossRef]
8. Ravel, B.; Newville, M. ATHENA, ARTEMIS, HEPHAESTUS: Data analysis for X-ray absorption spectroscopy using IFEFFIT. *J. Synchrotron Radiat.* **2005**, *12*, 537–541. [CrossRef] [PubMed]
9. Ravel, B. Artemis: EXAFS Data Analysis Using Feff with Larch or Ifeffit—Artemis 0.9.26 Documentation. 2016. Available online: https://bruceravel.github.io/demeter/documents/Artemis/index.html (accessed on 1 December 2021).
10. The FEFF Project-FEFF. Available online: http://monalisa.phys.washington.edu/feffproject-feff.html (accessed on 1 December 2021).

11. Vicat, J.; Fanchon, E.; Strobel, P.; Qui, D.T. The structure of $K_{1.33}Mn_8O_{16}$ and cation ordering in hollandite-type structures. *Acta Cryst.* **1986**, *B42*, 162–167. [CrossRef]
12. Lima, F.H.B.; Calegaro, M.L.; Ticianelli, E.A. Electrocatalytic activity of manganese oxides prepared by thermal decomposition for oxygen reduction. *Electrochim. Acta* **2007**, *52*, 3732–3738. [CrossRef]
13. Lee, J.M.; Patil, S.B.; Kang, B.; Lee, S.; Kim, M.G.; Hwang, S.-J. Understanding the crucial role of local crystal order in the electrocatalytic activity of crystalline manganese oxide. *J. Mater. Chem. A* **2018**, *6*, 12565–12573. [CrossRef]
14. Yang, Z.; Ford, D.C.; Park, J.S.; Ren, Y.; Kim, S.; Kim, H.; Fister, T.T.; Chan, M.K.Y.; Thackeray, M.M. Probing the Release and Uptake of Water in α-$MnO_2 \cdot xH_2O$. *Chem. Mater.* **2017**, *29*, 1507–1517. [CrossRef]
15. Yamamoto, S.; Matsuoka, O.; Fukada, I.; Ashida, Y.; Honda, T.; Yamamoto, N. Using Atomic Force Microscopy to Image the Surface of the Powdered Catalyst KMn_8O_{16}. *J. Catal.* **1996**, *159*, 401–409. [CrossRef]
16. Gul, S.; Ng, J.W.D.; Alonso-Mori, R.; Kern, J.; Sokaras, D.; Anzenberg, E.; Lassalle-Kaiser, B.; Gorlin, Y.; Weng, T.-C.; Zwart, P.H.; et al. Simultaneous detection of electronic structure changes from two elements of a bifunctional catalyst using wavelength-dispersive X-ray emission spectroscopy and in situ electrochemistry. *Phys. Chem. Chem. Phys.* **2015**, *17*, 8901–8912. [CrossRef] [PubMed]
17. Calvin, S. *XAFS for Everyone*, 1st ed.; CRC Press: Boca Raton, FL, USA, 2013.
18. Momma, K.; Izumi, F. VESTA: A three-dimensional visualization system for electronic and structural analysis. *J. Appl. Crystallogr.* **2008**, *41*, 653–658. [CrossRef]
19. Nam, K.-W.; Kim, M.G.; Kim, K.-B. In Situ Mn K-edge X-ray Absorption Spectroscopy Studies of Electrodeposited Manganese Oxide Films for Electrochemical Capacitors. *J. Phys. Chem. C* **2007**, *111*, 749–758. [CrossRef]